Publication Year	2018
Acceptance in OA	2021-01-27T09:33:23Z
Title	Characterization of the NNVT capillary plate collimators
Authors	CERAUDO, FRANCESCO, Ge, J., EVANGELISTA, YURI, MULERI, FABIO, Hanqi, M., Zhao, X., Wei, X., FEROCI, MARCO
Publisher's version (DOI)	10.1088/1748-0221/13/09/P09020
Handle	http://hdl.handle.net/20.500.12386/30024
Journal	JOURNAL OF INSTRUMENTATION
Volume	13

Prepared for submission to JINST

Characterization of the NNVT capillary plate collimators

F. Ceraudo,[a,1] **J. Ge,**[b] **Y. Evangelista,**[a] **F. Muleri,**[a] **M. Hanqi,**[b] **X. Zhao,**[b] **X. Wei**[b] **and M. Feroci**[a]

[a] *INAF/IAPS,*
via del Fosso del Cavaliere, 100, Rome, Italy
[b] *North Night Vision Technology Co.,Ltd.*
2, Kangping Street, Jiangning District, Nanjing, Jiangsu Province, China

E-mail: francesco.ceraudo@iaps.inaf.it

Abstract: In this paper, we report the results of the characterization campaign of two prototypes of Micro-Channel Plates (MCPs), designed as the X-ray collimators for the Large Area Detector on board the eXTP mission. The devices were developed ad-hoc by North Night Vision Technology Co., Ltd. (Nanjing, China). Measurements involved the study of the angular response (*rocking curve*) of each device to X-rays of different energies. The study evidenced how the angular response of a collimator changes with the energy of the incoming photons, with the onset of *side lobes* at high energy, which enlarge the effective field of view of the device, causing a potential contamination of the on-axis signal. Nevertheless, the magnitude of this effect is proven to be acceptable in most situations of astrophysical interest. On the lower hand of the energy spectrum, photons may also modify angular response due to grazing reflection on the inner walls of the collimator, a phenomenon strongly dependent on the degree of roughness of the surfaces involved. The whole campaign took place at the INAF/IAPS laboratories in Rome.

Keywords: eXTP, LAD, X-ray astronomy, space instrumentation, MCP

---

[1] Corresponding author.

Contents

1 Introduction

The *enhanced X-ray Timing and Polarimetry* (eXTP) mission is a space-borne mission currently under study of the Chinese Academy of Sciences and whose consortium includes institutions from China and most ESA members [13]. The scientific payload will carry state-of-the-art instruments for simultaneous spectral-timing studies of matter under extreme conditions of gravity, density and magnetism.

Among the scientific instruments on board eXTP is the *Large Area Detector* (LAD), an X-ray detector operating in the $2 - 30\,\mathrm{keV}$ energy range with an astonishing effective area of $\sim 3.4\,\mathrm{m}^2$ at 6 keV. Such an enormous area prevents the LAD from being placed at the focal plane of some focusing X-ray optics. Instead, it is composed of 40 modules featuring a set of 4×4 large-area Silicon Drift Detectors (SDDs) whose Field of View (FoV) is limited by lead-glass collimators.

In this paper, we will be discussing the characterization campaign of two prototypes of the LAD collimators, both developed by North Night Vision Technology (NNVT) Co., Ltd., (Nanjing, China). The tests took place at the INAF/IAPS laboratories in Rome. Their main aim was the evaluation of the FoV of each prototype, in order to assess how astrophysical sources outside the FoV could contaminate the measurements, and, in general, the contributions to the background and how they can be reduced.

2 Physical characteristics

The collimators are 5 mm-thick circular samples, with a 33 mm diameter. They are both based on the round-pore Micro-Channel Plate (MCP) technology. By design, the diameter of the channels is 83 µm and the Open Area Ratio (OAR) is 71 %. The channels are arranged in a hexagonal fashion. Collimators based on the MCP technology were previously employed on the Medium Energy (ME) instrument on board the EXOSAT mission [12].

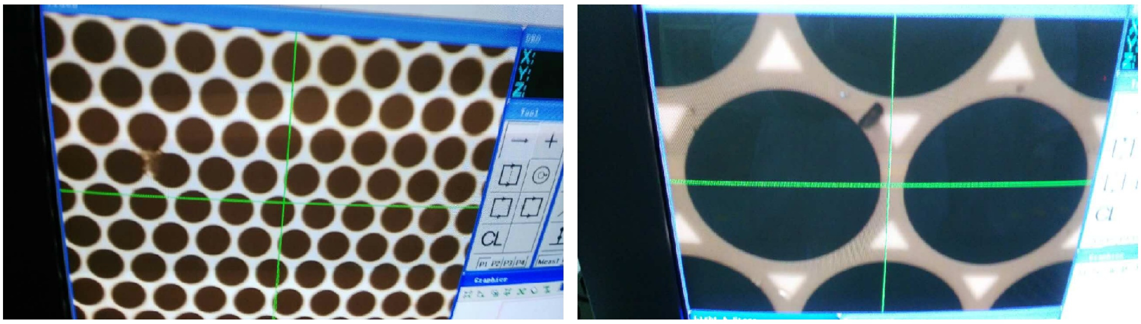

(a) **(b)**

Figure 1: *a)* Hexagonal disposition of the MCP channels. *b)* Lead inserts (white triangles) are nested among the pores to enhance absorption at certain angles.

The two prototypes differ for their structure and chemical composition. One (hereafter referred to as *sample I*) has a bulk made of 27%-rich lead glass, while 55%-rich triangular lead inserts are placed among the pores. The other one (hereafter, *sample II*) is made of 39 %-rich lead glass and has no lead-rich inserts. Figure 1a shows the layout of both the MCPs, while figure 1b is a close-up on the first one, showing the high-Z inserts. The characteristics of the samples are listed in table 1.

Table 1: List of physical properties of the MCP.

Sample	Diameter	Thickness	Pore diameter	OAR	Pb-fraction		Roughness
	mm	mm	µm		Bulk	Inserts	nm
I	33	5	83	71%	27%	55%	1
II	33	5	83	71%	39%	-	5

3 Angular response

In the following, we describe the data acquisition and analysis of the angular response curves of the MCP collimators. This was done by measuring the *rocking curves*, i.e. the number of photons transmitted by the collimator as a function of the angle between the photon direction and the normal to the MCP. Data were acquired using photons of two energies (20 keV and 6.4 keV) and in different geometrical configurations.

After an overview on the experimental setup (section 3.1), each curve is extensively analyzed and discussed in section 3.2 and 3.3 respectively.

3.1 Experimental setup

The photon beam for the study of the off-axis response of the MCP was generated by an X-ray tube – model Oxford, series 5000 – with different anodes depending on the required energy. The tube was positioned on a motorized linear stage – model Newport IMS500CC – and a manual vertical stage to enable alignment.

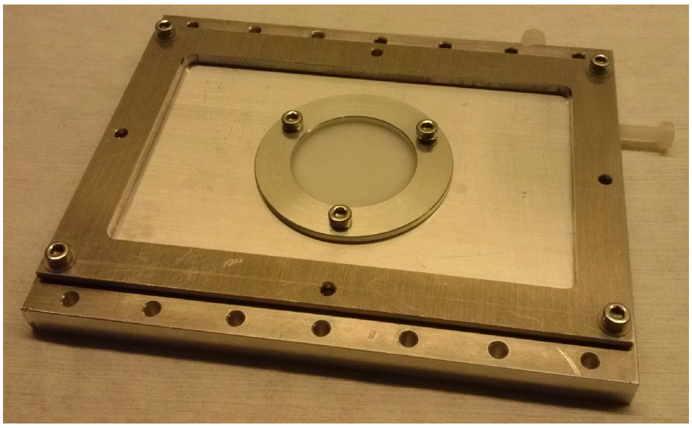

Figure 2: Picture of one of the NNVT *Micro Channel Plates* (MCPs) mounted on its holder to be handled during the measurements.

The MCP was installed on an aluminum holder (figure 2) and mounted on a rotation stage – model Newport RVS80CC –, which could be rotated with a < 10 arcsec precision to change the off-axis angle at which the photons impinged on the MCP. The stage was in turn fixed on a motorized rail – model Newport ILS250CC – to refine the alignment. X-ray photons passing through the MCP were eventually detected by an Amptek XR100CR Silicon-PIN detector with a $25\,\mathrm{mm}^2 \times 0.5\,\mathrm{mm}$ sensitive volume. The detector was mounted on manual vertical stage.

The alignment procedure consisted of several steps.

1. The X-ray tube (figure 3, *red*) and the detector (figure 3, *green*) were aligned in order to define the *optical axis* of the system.

2. A portable optical laser was used to simulate the X-ray beam during the rest of the alignment procedure.

3. Thanks to two diaphragms (100 µm and 500 µm respectively – figure 3, *blue*) and the motorized linear stage, the MCP (figure 3, *yellow*, and figure 4 in detail) is positioned with its center on the optical axis. We estimated that with our setup the alignment between the center of the MCP and the X-ray beam was ≈ 10 arcmin. In fact, this is done by alternatively moving the two diaphragms along a direction orthogonal to the optical axis, through their respective linear stages, and measuring the displacement that still allowed the laser to make its way to the MCP (≈ 2.1 mm and ≈ 2.6 mm respectively). By summing the two values in quadrature and dividing them by the distance between the diaphragms (≈ 1.155 m), the aforementioned rough estimate of ≈ 10 arcmin was obtained for the angular uncertainty of the alignment.

4. To make sure that the plane of the collimator was orthogonal to the optical axis, the MCP was oriented in such a way that it reflected back the laser spot, the latter being made visible through a target. This method assumed that the channels were orthogonal to the reflective surface (there was no information about that at this stage). We estimated an uncertainty of ≈ 8 arcmin, knowing the distance between the MCP and the target and the dimensions of the latter.

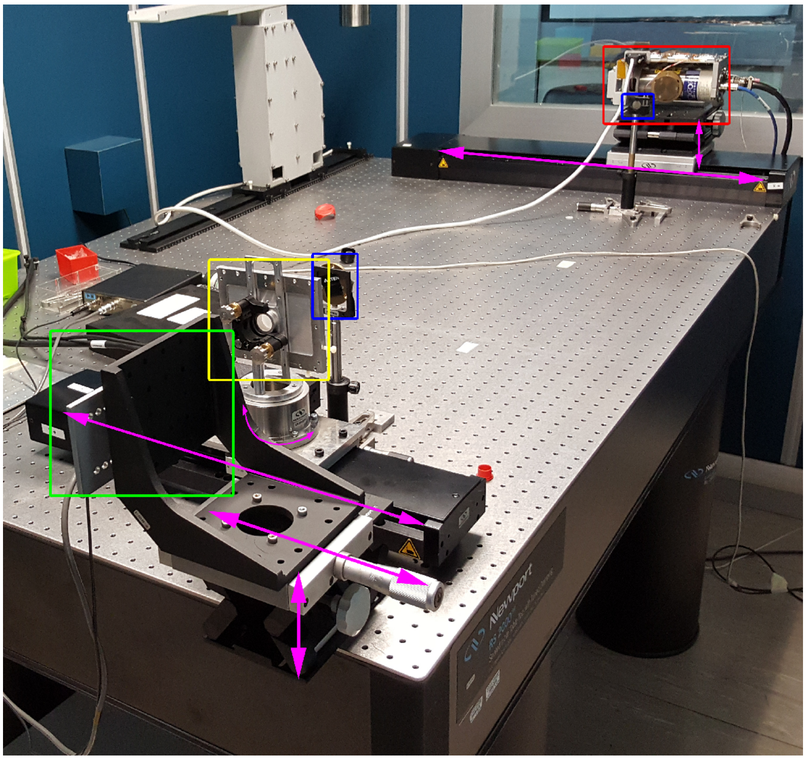

Figure 3: Experimental setup: X-ray tube (red), diaphragms (blue), MCP (yellow), detector (green), motorized/manual stages (magenta).

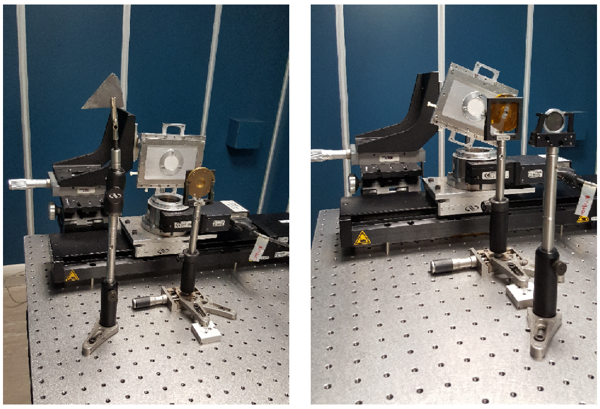

(a)

(b)

Figure 4: Two close-ups of one MCP mounted on its holder and movement stages. The 100 µm-diaphragm and the holder of the detector are visible in front of and behind the MCP respectively. The two configurations differ by a ≈ 10°-angle tilt. The second picture also show a silver filter to absorb the Bremsstrahlung continuum (see text).

5. Eventually, the X-ray tube and the detector were finely aligned along the axis, thanks to the motorized and manual moving stages (figure 3, *magenta*).

To limit the amount of photons scattered by the objects surrounding the optical system, and

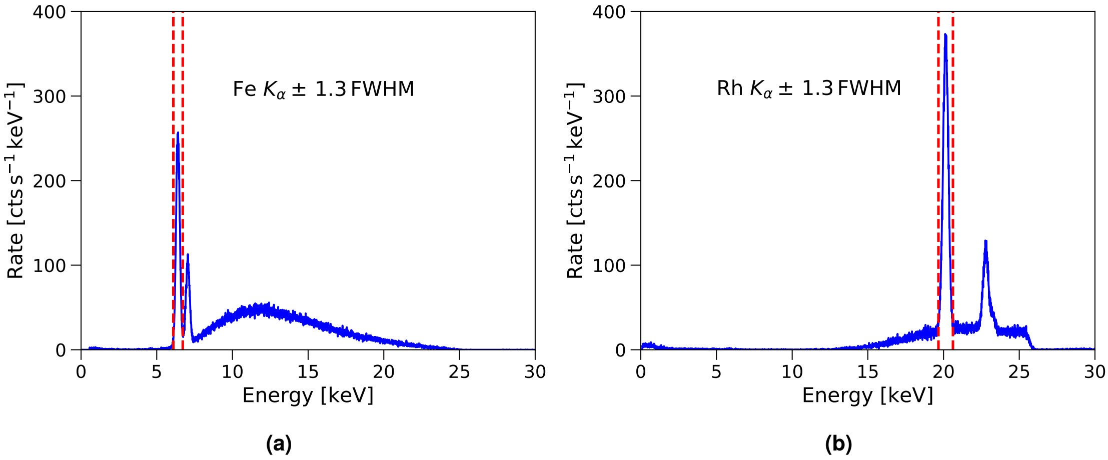

Figure 5: The spectra emitted by the X-ray tubes with the MCP in *zero-position*, i.e. with the channels parallel to the light beam. The K_α and K_β lines are clearly superimposed to the Bremsstrahlung continuum. Both plots show the energy bands used to measure each rocking curve. *a)* Fe anode. *b)* Rh anode: in this case an Ag filter is used to reduce the continuum and limit the rate of the photons on the detector (thus avoiding dead time).

thus reaching the detector without crossing the collimator, some lead blocks were stacked on both sides of the tube window. In addition, a 2 mm diaphragm was placed at the tube window, which already reduced the spot to 100 µm. This latter diaphragm also facilitated the alignment procedure.

An Iron (Fe) and a Rhodium (Rh) anode were used in the X-ray tube to provide photons at their K_α fluorescence lines, 6.4 keV and 20 keV respectively. The filament current and the high voltage of the tube were selected in order to maximize the signal and reduce dead time. For this reason, in the case of the Rh anode, a silver filter was positioned across the beam to absorb most of the Bremsstrahlung continuum, while leaving the fluorescence lines unchanged. The resulting spectra are shown in figure 5.

For each MCP prototype, a curve at 6.4 keV and two curves at 20 keV were acquired, the two 20 keV curves differing by a $\approx$ 10°-angle tilt, as shown in figure 4. The acquired curves are depicted in figure 6 and figure 7.

3.2 The high-energy rocking curve

The response $R(\theta)$ of a cylindrical collimator is given by [8]:

$$R(\theta) = \frac{1}{\pi}\left\{\phi - \frac{1}{2}\sin(2\phi) + K^2\left[\gamma - \frac{1}{2}\sin(2\gamma)\right]\right\} \tag{3.1a}$$

$$(\phi, \gamma) = \begin{cases} \cos\phi + K\cos\gamma - \frac{d}{r} = 0 \\ \sin\phi - K\sin\gamma = 0 \end{cases} \tag{3.1b}$$

$$d = L\tan\theta, \tag{3.1c}$$

where r and L are the pore radius and length respectively, θ is (the absolute value of) the off-axis or *rocking* angle, and ϕ and γ are defined in figure 8. K describes how far the source and the collimator

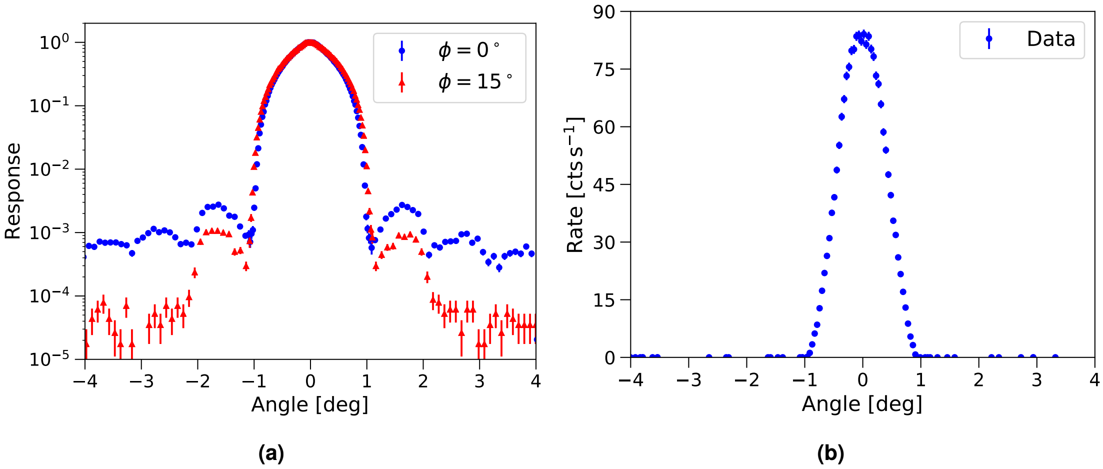

Figure 6: Measured rocking curves of the first MCP prototype. *a)* 20 keV-curve, with their respective tilt indicated. *b)* 6.4 keV-curve.

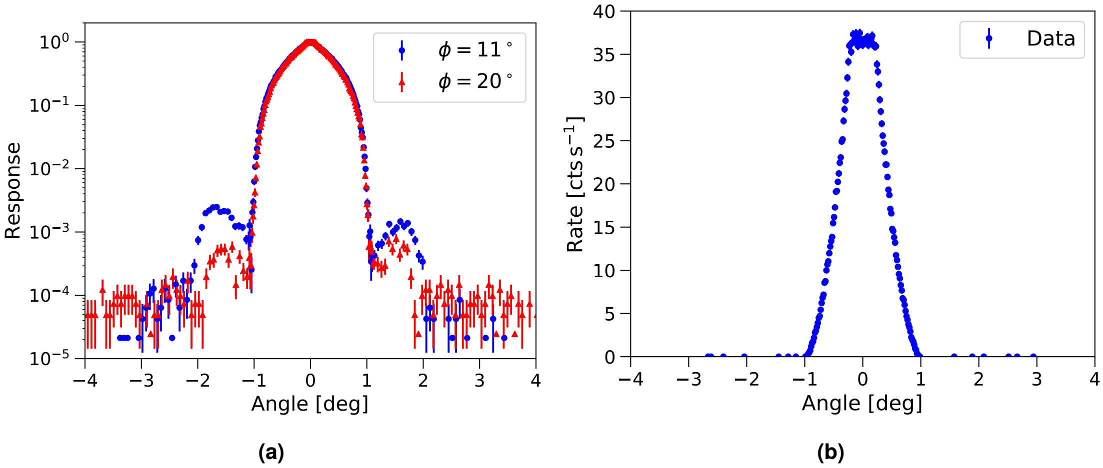

Figure 7: Measured rocking curves of the second MCP prototype. *a)* 20 keV-curves, with their respective tilt indicated. *b)* 6.4 keV-curve.

are from each other, and, with reference again to figure 8, it writes

$$K = \frac{z + L}{z}. \tag{3.2}$$

If the two elements are very far apart, then the beam is parallel and $K = 1$, otherwise $K > 1$.

We shall now discuss the origin of the side lobes clearly visible in figure 6a and 7a, and why they appear only at 20 keV while remaining undetected at 6.4 keV.

Let us consider a photon entering one of the pores of the MCP. The probability of it reaching the bottom of the channel is given by (3.1). However, if its energy is high enough, it can leak through the walls and enter a nearby channel: this phenomenon is modeled by an exponential damping of the response proportional to the distance the photon traverses through the wall. If the contribution of

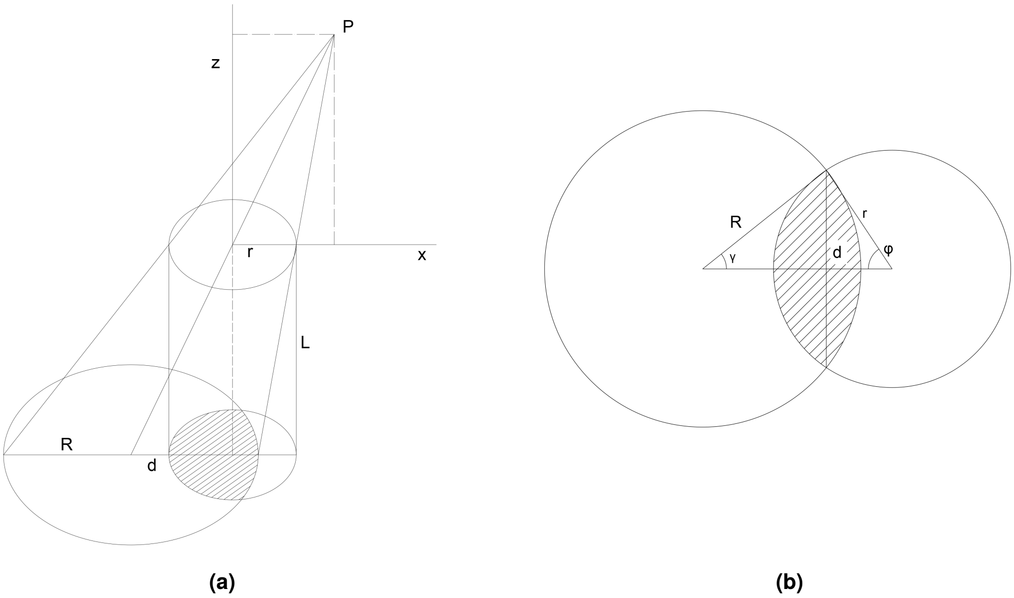

Figure 8: Definition of the angles ϕ and γ. *a)* If the source and the collimator are separated by a finite distance, then a circle of radius $R = Kr$ is projected, the distance between its center and the center of the channel being d (called E in the figure). *b)* The etched area is the overlapping zone between the channel cross-section (radius r) and the projected area (radius R). Again, the distance between the centers is indicated as E, while we refer to it as d in the text. [8]

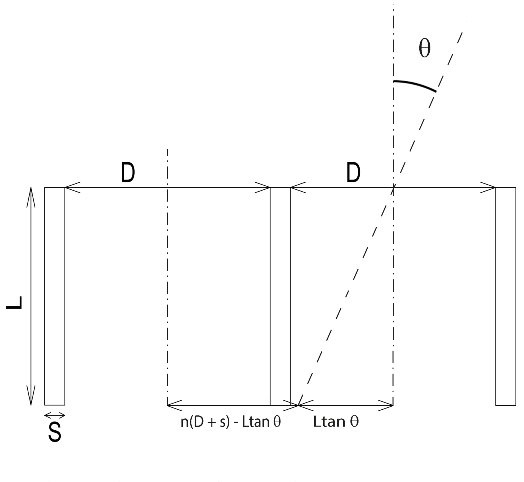

Figure 9: Definition of some relevant lengths of the collimator in its schematic cross-section. It is clear that $d_n = \left|n(D+s) - L\tan\theta\right|$ represents the distance between the center of the n-th pore ($n(D+s)$) and the point where the beam crosses the bottom of the collimator ($L\tan\theta$).

all the MCP channels is taken into account, one arrives at the following expression for the response $\epsilon(\theta, E)$ of a collimator

$$\epsilon(\theta, E) = \sum_{n=0}^{N} R_n(\theta) e^{-\mu(E)\rho \frac{ns}{\sin\theta}}, \tag{3.3}$$

where

$$R_n(\theta) = \frac{1}{\pi}\left\{\phi_n - \frac{1}{2}\sin(2\phi_n) + K^2\left[\gamma_n - \frac{1}{2}\sin(2\gamma_n)\right]\right\}, \tag{3.4a}$$

$$(\phi_n, \gamma_n) = \begin{cases} \cos\phi_n + K\cos\gamma_n - \frac{d_n}{r} = 0 \\ \sin\phi_n - K\sin\gamma_n = 0 \end{cases} \tag{3.4b}$$

$$d_n = \left| n\big(D + s\big) - L\tan\theta \right| \tag{3.4c}$$

with θ satisfying

$$L\tan\theta + Kr \geq n\big(D + s\big) - r \tag{3.5a}$$

$$L\tan\theta - Kr < n\big(D + s\big) + r. \tag{3.5b}$$

In the previous formulas, $|\cdot|$ indicates the absolute value and all the symbols retain their meaning from (3.1), whereas N is the total number of channels we are considering, s is the MCP frame thickness, and ρ and $\mu(E)$ are the density and the absorption coefficient of the material that constitutes the plate.[1] We point out that 3.4b has no solution for some values of d_n. It can be shown that d_n must comply with

$$d_n^4 + K^2(K^2 - 2) - 2d_n^2(1 + K^2) \leq -1. \tag{3.6}$$

To understand the physical meaning of this condition, we can consider figure 8 and 9. It is easy to see that, for any given n, d_n is the distance between the two circles in figure 8b. If θ (i.e. d_n) is such that the two circles do not intersect, then there is no pair (ϕ_n, γ_n) satisfying (3.4b).

Figure 10 shows the results of such calculations at different energies and *azimuth angle* (see below for further details). The occurrence of the side lobes is a direct consequence of the different amount of MCP frame material that X-rays cross as their direction changes with respect to the axis of the collimator.

The response of the collimator according to (3.3) strongly depends on the absorption $\mu(E)$, the density ρ and the frame thickness s. In the following, while both the density ρ and the frame thickness s are left free to vary, we adopt the absorption coefficient $\mu(E)$ of the Phillips 3502 glass, because of its chemical similarity with the one of the MCPs under study, as well as its availability in literature (table 2). Moreover, we take the absorption coefficient constant throughout the 20 keV-band (figure 5) and equal to the central value at 20 keV.[2] Figure 11 shows the 3502 glass absorption coefficient as a function of energy, while figure 10a shows the corresponding evolution of the MCP response.

---

[1] The exact number of bins involved in the curve is $2N - 1$, because we are not taking into account the sign of θ.

[2] The values of the absorption coefficient are retrieved from `physics.nist.gov/PhysRefData/Xcom/html/xcom1.html`, by using the 3502 glass pseudomolecule (table 2).

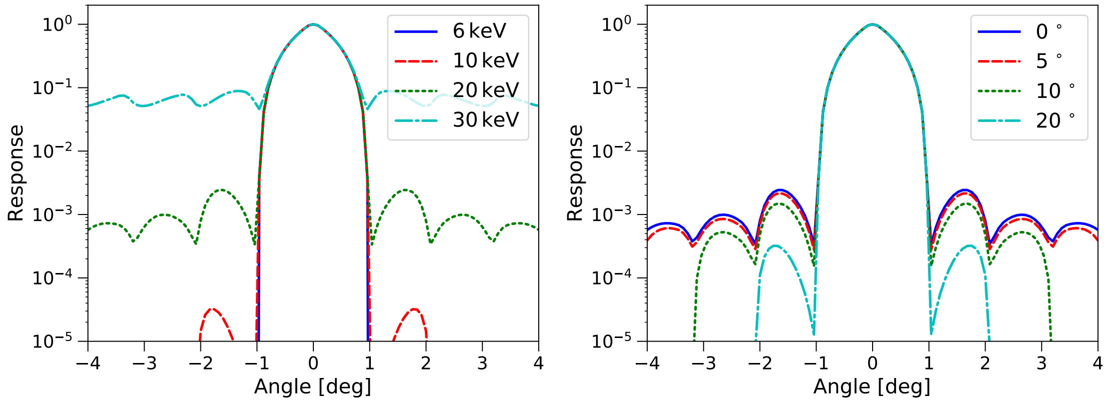

(a) **(b)**

Figure 10: Complete response of a collimator, as described by (3.3). *a)* Response at $\phi = 0°$ for different photon energies ($E = 6\,\mathrm{keV}, 10\,\mathrm{keV}, 20\,\mathrm{keV}, 30\,\mathrm{keV}$). *b)* Response at $E = 20\,\mathrm{keV}$ for different azimuth angles ($\phi = 0°, 5°, 10°, 20°$). Due to the hexagonal fashion of the arrangement of the channels, the response has a 30° periodicity in ϕ (figure 12).

Table 2: Chemical composition of Phillips 3502 glass according to [9]. If we compare this table with the data in table 1, one can see that the PbO component in the Phillips 3502 glass (27.4%) is not exactly the same as the nominal amount of lead in the bulk of the MCP (39%).

Composition by weight	Pseudomolecule	Density
49.4% SiO_2, 7.6% K_2O 27.4% PbO, 4.59% Na_2O 11% Bi_2O_3, 0.05% BaO	$Si_5O_{12}PbKNa$	$3.3\,\mathrm{g\,cm^{-3}}$

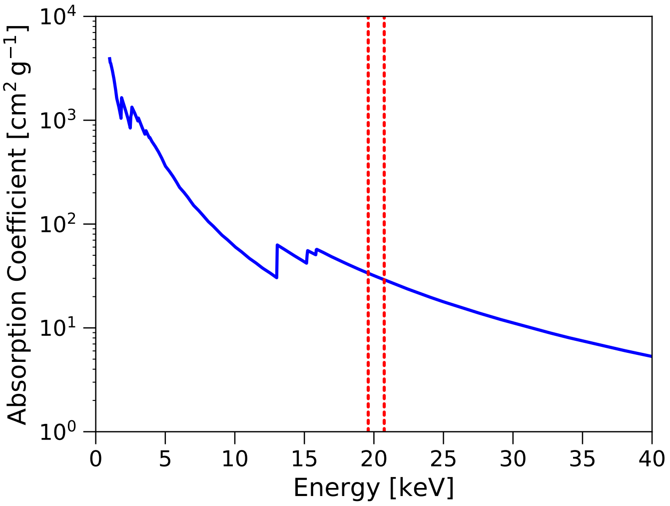

Figure 11: Absorption coefficient of 3502 glass as a function of energy. The 20 keV-band of figure 5b is highlighted in dotted lines.

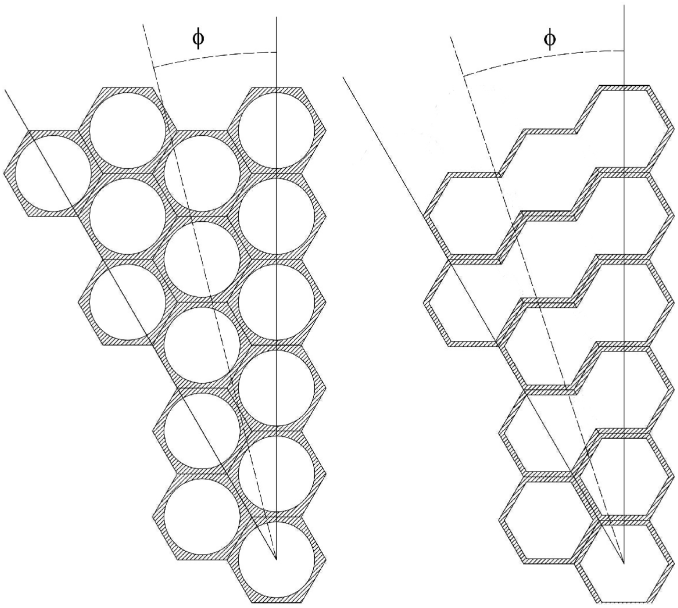

Figure 12: *Left:* Schematics of the cross-section of the MCP, with the cylindrical pores arranged in a hexagonal pattern. *Right:* Simplified version of the cross-section used to implement the dependence of the thickness on the azimuth angle ϕ, clearly indicated in both the figures, along with the 0° (vertical) and 30° lines.

It is important to also point out that the fame thickness s of (3.3) is in fact a function of the *azimuth angle* ϕ, i.e. the angle between the direction of the rocking curve scan and a reference orientation of the MCP pores. We must stress that ϕ must not be confused with the variables with the same name in (3.1a) and (3.3). Figure 12 illustrates the definition of ϕ and also how the model of the MCP is simplified to efficiently estimate the length of the photon path through the MCP frame. With this consideration, we can make the substitution

$$ns \longrightarrow s(\phi) \tag{3.7}$$

in the exponent of (3.3), whereas in the following s shall indicate the thickness of the boundary between two hexagonal cells of the model (i.e. the thickness of each horizontal trait at $\phi = 0°$ on the right of figure 12, or the minimum possible value of $s(\phi)$). Figure 10b illustrates how the MCP response varies with ϕ.

A lower limit for s (which may be a useful reference) can be estimated by considering that the pores are arranged in an hexagonal fashion. Since s is approximately the distance between two nearby channels, we can outline a scheme as the one in figure 13: from simple geometry, the circle's and the bigger hexagon's areas are expressed by

$$A_{\text{circ}} = \pi r^2 \tag{3.8a}$$

$$A_{\text{hex}} = 2\sqrt{3}(r+h)^2, \tag{3.8b}$$

which are related to each other by the *Open Area Ratio* (OAR):

$$\text{OAR} = \frac{A_{\text{circ}}}{A_{\text{hex}}} = \frac{\pi}{2\sqrt{3}}\left(\frac{r}{r+h}\right)^2. \tag{3.9}$$

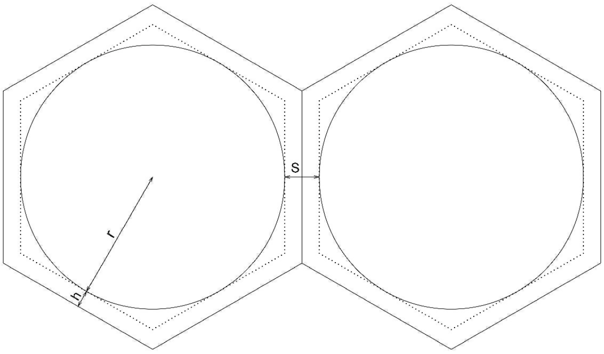

Figure 13: Schematics of the pore arrangement, with the definition of the reference lengths.

Since we know both the OAR of the MCP (OAR $\approx$ 70%) and the pore diameter $D = 8\,\mu\text{m}$, we can invert (3.9) and, considering that $s = 2h$ and $D = 2r$, obtain

$$s = \left(\frac{1}{\sqrt{\frac{2\sqrt{3}}{\pi}\text{OAR}}} - 1 \right) D, \tag{3.10}$$

corresponding to the rough estimate $s = 10.8\,\mu\text{m}$, which is the minimum frame thickness that can be intercepted by the X-ray photons.

The parameters describing the MCPs are extracted from the data through a Markov chain Monte Carlo (MCMC) [6] with Gaussian likelihood and uninformative prior. Since many of those are degenerate (e.g. s, ϕ and ρ), the following strategy was adopted to ensure the convergence of the algorithm.

- The response $R(\theta)$ of (3.1) was convolved with a Gaussian distribution $G(\theta; 0, \sigma)$ in order to take into account the misalignment of the MCP pores.
- The diameter $D = 83\,\mu\text{m}$ was fixed.
- The $\phi = 0°$ curve of the first sample was analyzed first, thus extracting an estimate for the frame thickness s, the channel length L, the glass density ρ and the pore misalignment σ. In the computations, $\phi = 0°$ was kept constant.
- The tilted curve of the first sample was then analyzed by using the results of the previous fit as fixed parameters and varying the azimuth angle ϕ instead.
- The procedure was iterated for the curves of the second sample, except s was always kept constant and equal to the value previously found, as the two prototypes have the same structure and otherwise the fit results would be poorly constrained. The azimuth angle ϕ of the first curve was fixed at the experimental value of 11°, and left free to vary in the case of the second curve.

Table 3: Fit results of the 20 keV-rocking curves of the first MCP prototype. Central values are to be intended as medians, whereas uncertainties give 95 % confidence intervals.

L	$5.058^{+0.020}_{-0.017}$ mm	σ	$1.53^{+0.12}_{-0.15}$ arcmin
ρ	$2.95^{+0.17}_{-0.17}$ g cm^{-3}	s	$15.38^{+1.02}_{-0.91}$ µm
ϕ_1	0°	ϕ_2	$13.90^{+3.4}_{-3.7}$ °

Table 4: Fit results of the 20 keV-rocking curves of the second MCP prototype. Central values are to be intended as medians, whereas uncertainties give 95% confidence intervals.

L	$4.760^{+0.030}_{-0.027}$ mm	σ	$2.09^{+0.21}_{-0.20}$ arcmin
ρ	$2.976^{+0.034}_{-0.034}$ g cm^{-3}	s	$15.38^{+1.02}_{-0.91}$ µm
ϕ_1	11°	ϕ_2	$20.78^{+0.68}_{-0.60}$ °

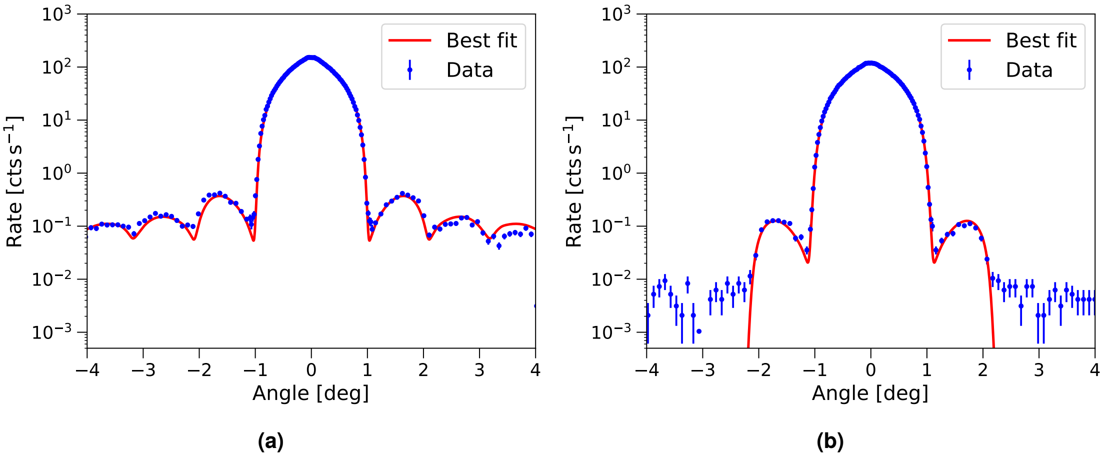

Figure 14: Fitted 20 keV-rocking curves of the first MCP prototype. *a)* 0°-tilt. *b)* 15°-tilt.

Table 3 and 4 summarize the fit results, which are plotted in figures 14 and 15. Hereafter, unless otherwise specified, central values are to be intended as medians, whereas uncertainties give 95% confidence intervals.

As shown in figure 15, the fit performed slightly worse on the second sample. The explanation of this is twofold: on the one hand, alignment issues or limitations in the uniformity of the movement of the rotational stage, since with the second collimator the rocking velocity was set lower than the first case, might have influenced the symmetry of the measured rocking curve; on the other hand, in the case of figure 15b, the height of the side lobes is comparable to the background level, resulting on a disappearance of features such as the neat separation between main and side lobes, that help to constrain the fit.

As far as the numerical results are concerned, the best-fit value of $s = 15.38^{+1.02}_{-0.91}$ µm is larger than the one derived with (3.10), which is consistent with the fact that 10.8 µm is the minimum distance between two pores. Moreover, the values of $L_1 = 5.058^{+0.020}_{-0.017}$ mm and $L_2 = 4.760^{+0.030}_{-0.027}$ mm

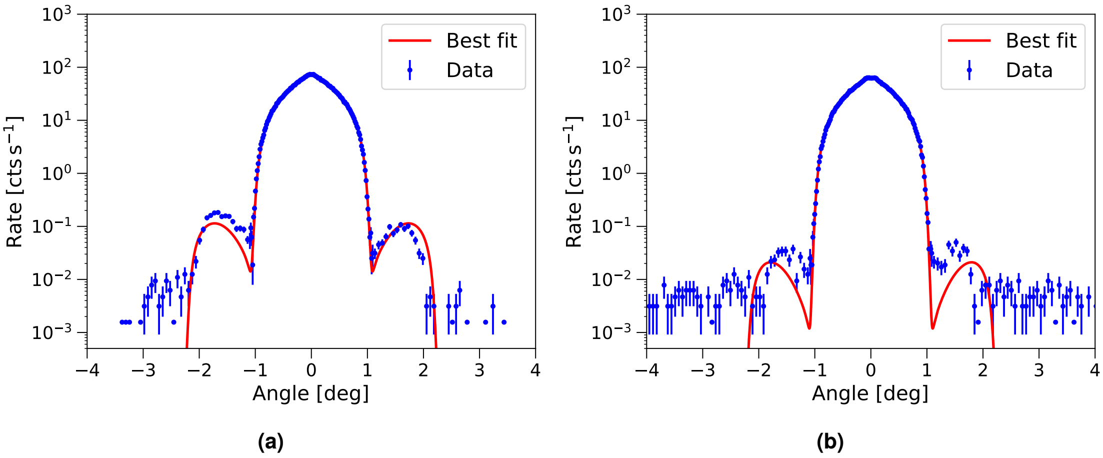

(a) **(b)**

Figure 15: Fitted 20 keV-rocking curves of the second MCP prototype. *a)* 10°-tilt. *b)* 20°-tilt.

are very close to the nominal value of 5 mm. It is also worth noting that, as the absorption is concerned, the two MCPs behaved equivalently. In fact, if we calculate the lead content of the first MCP by averaging the lead fractions of the bulk and the inserts, the weights being simply provided by their contribution to the surface area of the MCP itself (figure 1b), we find ≈ 39%, which is exactly the lead fraction of the second sample, whose composition is homogeneous throughout the frame. This is reflected in the two estimates for the glass densities derived from the fits ($\rho_1 = 2.95^{+0.17}_{-0.17}\,\mathrm{g\,cm^{-3}}$ and $\rho_2 = 2.976^{+0.034}_{-0.034}\,\mathrm{g\,cm^{-3}}$), which are compatible well within the uncertainties.

3.3 The low-energy rocking curve

The shape of the 6.4 keV-curve is very different from the analytic MCP response of (3.3) which was used to analyze the 20 keV-data in § 3.2. This is visible especially towards the peak of the response (figure 16). This phenomenon is likely to be caused by *photon reflection* on the inner walls of the MCP channels, as it is expected based on simulations like those in [11] and shown in figure 17. If this is the case, it also means that the walls are very well polished, as qualitatively suggested by the very large angle at which the measured curve departs from the quasi-triangular analytic response.

A ray-tracing algorithm was implemented to study the MCP response at low energy. For each value of the rocking angle θ, a number of photons are randomly generated across the entrance of the channel and then let propagate down the aperture (figure 18). If a photon reaches a wall, its grazing angle of incidence (which is equal to the rocking angle, because of the geometry of figure 18) is compared to the *critical angle* α_C, i.e. the angle below which total reflection occurs. The *critical angle* is defined as

$$\alpha_C = \arccos(n), \tag{3.11}$$

where n is the refractive index of the glass (figure 19).[3] The refractive index of the surrounding environment is taken equal to 1. If $\theta \leq \alpha_C$, the photon is reflected, otherwise it is absorbed and

---

[3] The refractive index as a function of energy was retrieved from `henke.lbl.gov/optical_constants/getdb2.html`, by using the 3502 glass pseudomolecule (table 2).

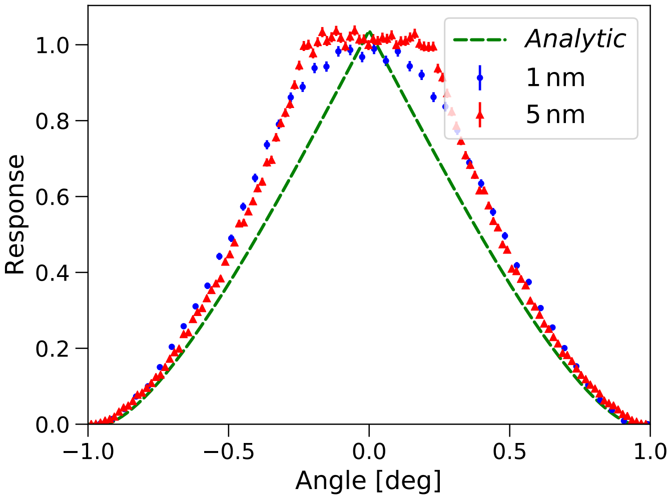

Figure 16: Comparison between the 6.4 keV response of the two MCPs and the response of (3.3) calculated at the same energy.

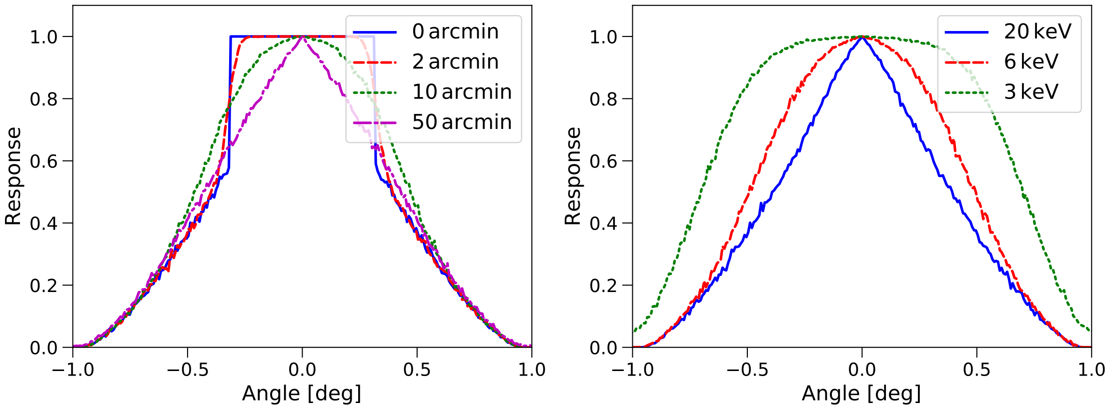

(a) **(b)**

Figure 17: Effect on the response of a collimator by inner-wall grazing reflection of photons, as simulated through the Monte Carlo algorithm explained in the text. *a)* Fixed energy (6.4 keV), variable roughness (expressed in arcmin). The *step-like* response due to the grazing reflection at 0 arcmin happens between $\pm\alpha_C$. Roughness acts like a gaussian smoothing on the step. *b)* Fixed roughness (6 arcmin), variable energy.

removed from the simulation. Once a photon is reflected, its trajectory is computed to verify whether it intercepts the other wall, in which case the occurrence of reflection is tested again. This process is repeated until the photon is either absorbed or detected. We consider a photon as being *detected* when it reaches the bottom of the channel without being absorbed. The final response of the collimator is calculated as the ratio of the number of *detected photons* and *total trials*.

An angle $d\theta$ accounts for the surface roughness of the inner walls: $d\theta$ is summed to the grazing (rocking) angle θ, whenever we test for reflection, so that the condition for reflection is implemented

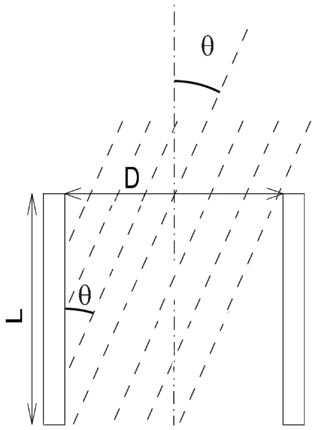

Figure 18: Scheme of the geometry of the two-dimensional ray tracing simulation. The tracks of some of the generated photons are indicated, as well as the relevant physical parameters of the collimator channel.

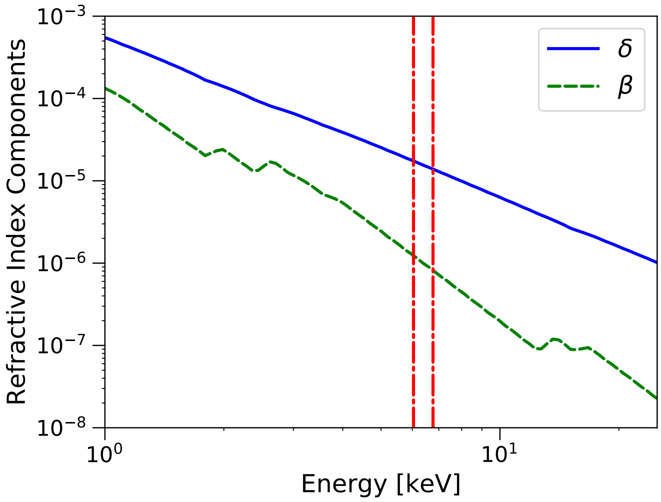

Figure 19: Refractive index components of the Phillips 3502 glass. The usual convention of the complex refractive index is applied, i.e. $n = 1 - \delta - i\beta$. The energy band over which the MCP calibration is carried out is highlighted as in figure 5a.

as

$$\theta + d\theta \leq \alpha_C. \tag{3.12}$$

The value of $d\theta$ is drawn from a normal distribution centered at zero and with a standard deviation corresponding to the rms value of the roughness (σ, expressed in arcmin).

The described procedure was included in a routine to perform a fit on the 6.4 keV-MCP data, again using a Markov Chain Monte Carlo [6] with uninformative prior. Results are reported in figure 20, table 5.

We can see that the fitted curve describes very well the data for both MCP samples, implying that all the deviations from the analytic response can be accounted for by the inclusion of photon

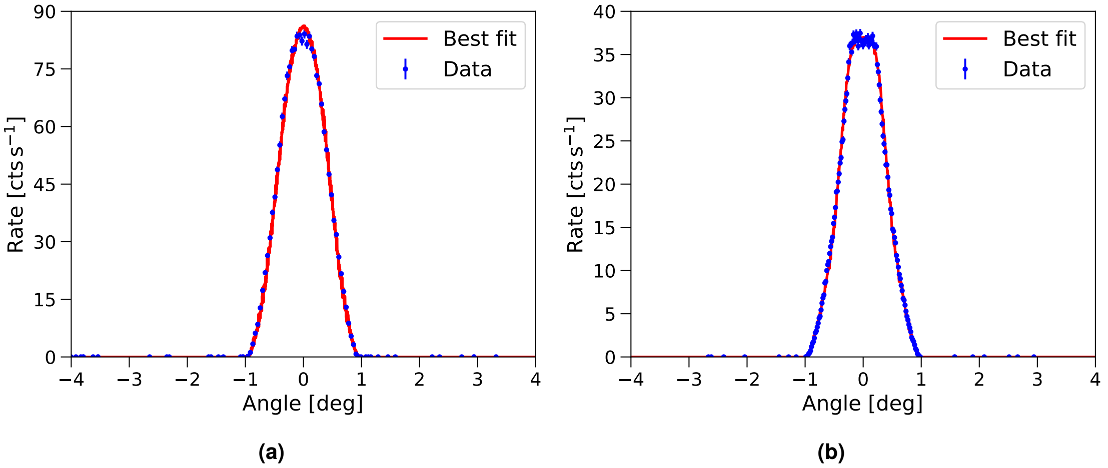

Figure 20: Fitted 6.4 keV-rocking curves. *a)* First prototype. *b)* Second prototype.

Table 5: Fit results of the 6.4 keV-rocking curves of the two MCP prototypes. Central values shall be intended as medians, whereas the interval between the lower and the upper uncertainty is a 95% confidence level.

I	L	$4.963^{+0.059}_{-0.067}$ mm	σ	$12.44^{+0.42}_{-0.43}$ arcmin
II	L	$4.855^{+0.047}_{-0.046}$ mm	σ	$6.84^{+0.19}_{-0.17}$ arcmin

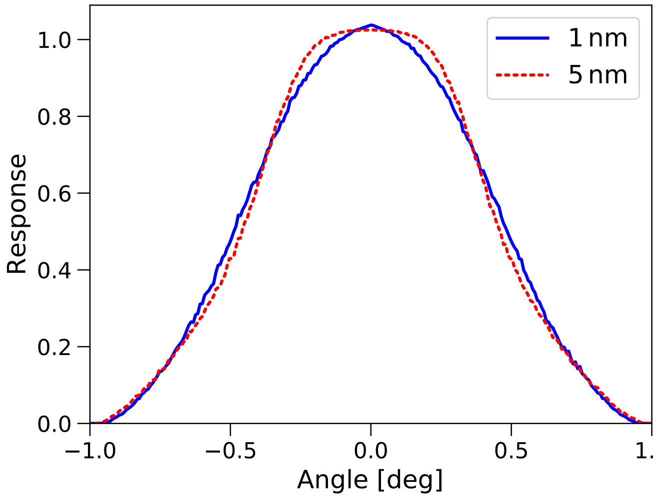

Figure 21: Comparison between the fitted responses at 6.4 keV of the two MCPs, normalized to their area. The two curves behave as in figure 17a according to the fitted σ, but contrary to the value by design of their roughness (in the legend).

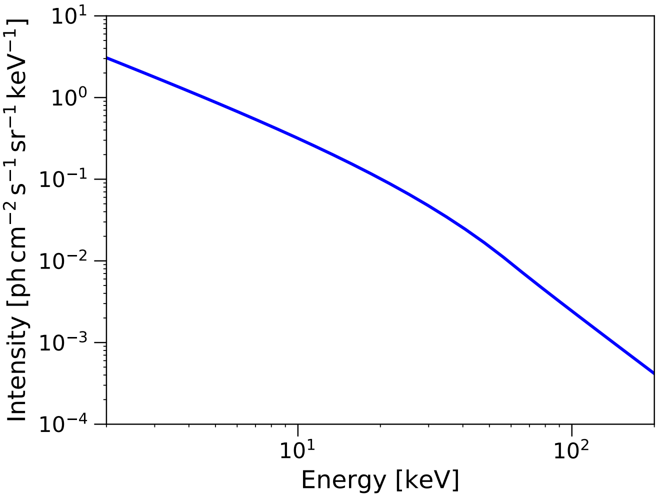

Figure 22: Spectrum of the Cosmic X-ray Background, as derived derived from HEAO-1 A4 and COMPTEL measurements [1, 7].

grazing reflection on the inner walls of the channels. However, when examining the best-fit values for σ, we find an unexpected result because $\sigma_1 > \sigma_2$. From figure 17a, one can see that, as σ increases, the influence of reflected photons on the response decreases, because grazing reflection becomes harder on a more rough surface, which is implemented as a wider Gaussian distribution of $d\theta$ in 3.12. This is exactly the behavior that is supposed to be seen experimentally, i.e. the more rough the surface the larger the value of σ. Nevertheless, as the fit results and figure 21 clearly show, the second MCP prototype, which was designed with a 5 nm surface roughness, features a larger influence of grazing reflection (flatter response near the top, smaller σ) than the first prototype, whose surface roughness is 1 nm by design. Further investigations are therefore required to completely address this point and verify the quality of the fabrication process.

4 The astrophysical background

As we studied in section 3, high energy photons can leak through the channel walls, leading to a response featuring not only a well-defined ±1° *main lobe*, which defines the FoV of the device, but also several smaller *side lobes* on both sides of the main lobe (figure 10). Even though the side lobes are always at least two orders of magnitude smaller than the main lobe, their presence results in out-of-FoV photons contaminating the in-FoV signal. In this section we will be providing an estimate of the contamination of the in-FoV signal in two configurations of astrophysical interest: photons from a diffuse source (the Cosmic X-ray Background) and from off-axis point-like sources.

We can try to estimate the contamination of the signal inside the FoV due to the photons of the *Cosmic X-ray Background* (CXB) leaking through the collimator from outside the FoV. For our calculations, we use the CXB model of [1, 7], derived from HEAO-1 A4 and COMPTEL measurements. Its analytic expression at energies $E \leq 60\,\mathrm{keV}$ is

$$F(E) = 7.877\,E^{-1.29} e^{-\frac{E}{41.3\,\mathrm{keV}}} \qquad \left[\mathrm{ph\,cm^{-2}\,s^{-1}\,sr^{-1}\,keV^{-1}}\right], \tag{4.1a}$$

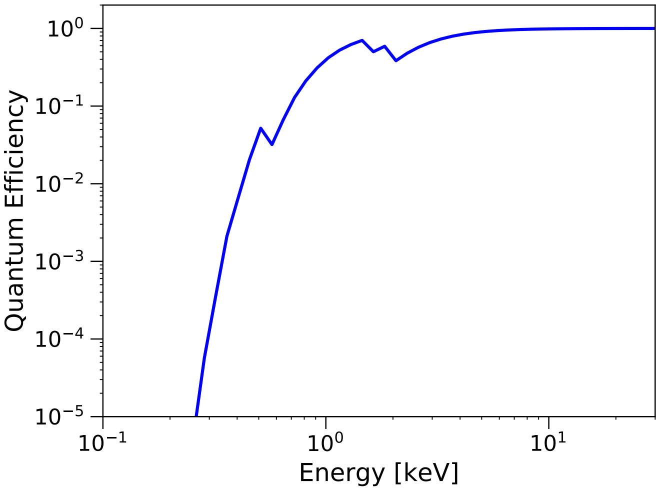

Figure 23: Energy-dependent quantum efficiency of the Silicon Drift Detectors (SDDs) below the collimator of the eXTP LAD.

whereas at $E > 60\,\mathrm{keV}$

$$\begin{aligned} F(E) &= 0.0004317\left(\frac{E}{60}\right)^{-6.5} \\ &+ 0.0084\left(\frac{E}{60}\right)^{-2.58} \\ &+ 0.00048\left(\frac{E}{60}\right)^{-2.05} \qquad \left[\mathrm{ph\,cm^{-2}\,s^{-1}\,sr^{-1}\,keV^{-1}}\right]. \end{aligned} \tag{4.1b}$$

The CXB spectrum is shown in figure 22.

The expected contamination in a defined energy band ΔE is given by the integral

$$C_{\mathrm{CXB}} = \int_{\Delta E} dE \int_0^{2\pi} d\phi \int_{1^\circ}^{90^\circ} \sin\theta d\theta\; F(E)\mathrm{QE}_{\mathrm{LAD}}(E)\epsilon(\theta,\phi,E) \qquad \left[\mathrm{cts\,cm^{-2}\,s^{-1}}\right] \tag{4.2}$$

with θ and ϕ being the rocking and the azimuth angle respectively, $\epsilon(\theta, \phi, E)$ the energy-dependent angular response of (3.3) with $s = s(\phi)$, $F(E)$ the specific intensity of (4.1a) and (4.1b) and $\mathrm{QE}_{\mathrm{LAD}}(E)$ the quantum efficiency of the LAD detector below the collimator, shown in figure 23. The integration along the rocking direction is carried out between $\theta = 1^\circ$ (FoV limit) and $\theta = 90^\circ$, although the response becomes negligible well before this second angle. In practice, the maximum acceptance angle will be limited by the structures surrounding the detector and by its finite dimensions. It is finally worth noting that, as our data analysis pointed out in § 3.2, the two samples are essentially equivalent, as far as their absorption is concerned (same wall thickness, geometrical arrangement of the pores and average density), thus the integral in (4.2) will provide the same values for the two prototypes.

The results are shown in table 6, where we report two contributions for each energy band:

- *Aperture* is the measured CXB flux *inside* the FoV, i.e. the output of (4.2) where the integration is performed over $0^\circ \leq \theta \leq 1^\circ$; this value is given as a reference;

Table 6: Contributions of the CXB to the LAD background. Central values shall be intended as medians, whereas the interval between the lower and the upper uncertainty is a 95% confidence level.

Contribution	$2-10\,\mathrm{keV}$		$2-30\,\mathrm{keV}$	
	$\mathrm{cts\,cm^{-2}\,s^{-1}}$	mCrab	$\mathrm{cts\,cm^{-2}\,s^{-1}}$	mCrab
Aperture	$1.4386^{+0.0082}_{-0.0232} \times 10^{-3}$	$0.6572^{+0.0037}_{-0.0106}$	$2.068^{+0.012}_{-0.033} \times 10^{-3}$	$0.7753^{+0.0044}_{-0.0125}$
Leaking	$4.42^{+0.24}_{-0.21} \times 10^{-9}$	$2.021^{+0.109}_{-0.095} \times 10^{-6}$	$5.62^{+0.45}_{-0.57} \times 10^{-4}$	$0.211^{+0.017}_{-0.021}$

- *Leaking* is the result of (4.2), i.e. the flux of CXB photons *leaking* through the channel walls.

Each number is also presented in units on mCrab: for the unit conversion, we considered the spectrum of the Crab as given by [10]:

$$N(E) = N_\gamma\, E^{-\Gamma} e^{-N_H\,\sigma_{\mathrm{ph}}}, \tag{4.3}$$

with $N_\gamma = 8.97\,\mathrm{ph\,cm^{-2}\,s^{-1}\,keV^{-1}}$, $\Gamma = 2.08$, $N_H = 4.5 \times 10^{21}\,\mathrm{cm^{-2}}$, and abundances and photoelectric cross-sections given by [2] and [3, 4] respectively.

We can compare these results to those in [5], where the CXB-induced contamination level was estimated as $7.4 \times 10^{-3}\,\mathrm{cts\,cm^{-2}\,s^{-1}}$ in the $2-30\,\mathrm{keV}$. Our analysis provided a result which is $\approx 8\%$ this value, which is acceptable since no reprocessing of high-energy photons was included in our calculations: indeed, unlike [5], we did not take into account cosmic photons which are reprocessed into the $2-30\,\mathrm{keV}$ due to phenomena such as Compton scattering or fluorescence.

In the case of point-like sources, the value of the response at discrete angles becomes important, because the photons from each source come at specific off-axis angles. From figure 10, one can see that the first side lobe is always the dominant one, no matter the energy E or the azimuth ϕ, and that its peak value may vary over some orders of magnitude depending on E and ϕ, but it is at most 0.1 times the peak of the main lobe, if we limit ourselves to $E \leq 30\,\mathrm{keV}$. As a reference, we can list the values of the response for selected angles, at fixed energy and azimuth:

$$\begin{aligned}
\epsilon(\theta = 1.65°, \phi = 0°, E = 20\,\mathrm{keV}) &= 2.45 \times 10^{-3} \\
\epsilon(\theta = 30°, \phi = 0°, E = 20\,\mathrm{keV}) &= 1.84 \times 10^{-4} \\
\epsilon(\theta = 60°, \phi = 0°, E = 20\,\mathrm{keV}) &= 3.52 \times 10^{-7}.
\end{aligned}$$

It is clear that, when a strong off-axis source is within $1° - 2°$ from the FoV, its contamination is significant (an unlikely situation for observations with the LAD), but its importance rapidly decreases with the off-axis angle, becoming essentially negligible already at 30°. It is worth noting that those results become more (less) favorable as the energy decreases (increases), as visible in figure 10a, due to the energy dependence of $\epsilon(\theta, \phi, E)$. In addition, we point out that we again neglected the background reprocessing at the considered energy, such as Earth γ-ray or neutron emission, cosmic rays or CXB-induced effects (e.g. fluorescence and Compton) which is by far the dominant component.

5 Conclusions

We reported the results of the characterization campaign of two prototypes of Micro-Channel Plates, developed ad-hoc by North Night Vision Technology Co., Ltd. The angular response of both devices was investigated at 20 keV and 6.4 keV (Rh and Fe K_α lines respectively).

The results of the higher-energy tests showed that energetic off-axis photons may cross the walls of the collimators and thus be detected. This phenomenon causes the rocking curve to feature a main lobe as wide as the intended FoV of the MCP, along with several side lobes, whose contribution varies according to the energy of the photons and their specific direction of propagation (figure 10). This fact is a source of contamination. However, we showed that this contribution is acceptable in the case of an extended background source, such as the CXB, or even in case of strong point-like sources, provided that they are not within $1^\circ - 2^\circ$ from the FoV.

The analysis of the lower-energy rocking curve highlighted that the energy of photons is too low for them to cross the channel walls, implying that no side lobe is detected. However, in this energy range, another phenomenon affects the response, i.e. grazing reflection on the inner walls of the channels (figure 16). Grazing reflection causes the response close to $\theta = 0^\circ$ to flatten, and more generally it makes the contribution of the angular regions near the center of the FoV more important (figure 16). This affects the performance of the MCP by increasing the background at low energies. From this respect, our analysis revealed a puzzling result, i.e. the observed impact of the grazing reflection on the response seems to be larger in the second prototype, whose inner walls were designed more rough than the first. This point must be further investigated to ascertain the correctness of the fabrication process.

References

[1] M. Ajello, J. Greiner, G. Sato, et al., *Cosmic X-ray Background and Earth albedo spectra with Swift BAT*, *ApJ* **689** (2008) 666.

[2] E. Anders. & N. Grevesse, *Abundances of the elements - Meteoritic and solar*, *Geochim. Cosmochim. Acta* **53** (1989) 197-214.

[3] M. Balucinska-Church & D. McCammon, *Photoelectric absorption cross sections with variable abundance*, *ApJ* **400** (1992) 699.

[4] M. Yan, H. R. Sadeghpour & A. Dalgarno, *Photoionization Cross Sections of He and* H_2, *ApJ* **496** (1998) 1044-1050.

[5] R. Campana, M. Feroci, E. Del Monte, et al., *Background simulations for the Large Area Detector onboard LOFT*, *Exp. Astron.* **36** (2013b) 451-477.

[6] D. Foreman-Mackey, D. W. Hogg, D. Lang, & J. Goodman, *emcee: The MCMC Hammer*, *Pub. of the ASP* **125** (2013) 306-312 [arXiv:1202.3665].

[7] F. Frontera, M. Orlandini, R. Landi, et al., *The Cosmic X-ray Background and the population of the most heavily obscured AGNs*, *ApJ* **666** (2007) 86.

[8] G. E. Gigante, *A new approach to evaluate the response functions for conical and cylindrical collimators*, *Nucl. Instrum. Meth. Phys. Res. B* **275** (1989) 397-402.

[9] G. W. Fraser, *The soft X-ray quantum detection efficiency of microchannel plates*, *Nucl. Instrum. Meth.* **195** (1982) 523-538.

[10] M. G. Kirsch, et al., *Crab: the standard X-ray candle with all (modern) X-ray satellites*, *Proc. SPIE* **5898** (2005) 22-33.

[11] T. Mineo, et al., *Effects of capillary reflection in the performance of the collimator of the Large Area Detector on board LOFT*, *Ex. Astron.* **37** (2014) 69-84.

[12] M. J. L. Turner, A. Smith & H. U. Zimmermann, *The medium energy instrument on EXOSAT*, *Space Sci. Rev.* **30** (1981) 513-524.

[13] S. N. Zhang, et al., *eXTP: Enhanced X-ray Timing and Polarization mission*, *Proc. SPIE* **9905** (2016) 99051Q.